Liquid-Phase Exfoliation of Phosphorene: Design Rules from Molecular Dynamics Simulations

Vishnu Sresht,[†] Agílio A. H. Pádua,[*,†,‡] and Daniel Blankschtein[*,†]

[†]Department of Chemical Engineering, Massachusetts Institute of Technology, Cambridge, Massachusetts 02139, United States and [‡]Institut de Chimie de Clermont-Ferrand, Université Blaise Pascal and CNRS, 63171 Aubiére, France

ABSTRACT The liquid-phase exfoliation of phosphorene, the two-dimensional derivative of black phosphorus, in the solvents dimethyl sulfoxide (DMSO), dimethylformamide (DMF), isopropyl alcohol, *N*-methyl-2-pyrrolidone, and *N*-cyclohexyl-2-pyrrolidone is investigated using three molecular-scale "computer experiments". We modeled solvent—phosphorene interactions using an atomistic force field, based on *ab initio* calculations and lattice dynamics, that accurately reproduces experimental mechanical properties. We probed solvent molecule ordering at phosphorene/solvent interfaces and discovered that planar molecules such as *N*-methyl-2-pyrrolidone preferentially orient parallel to the interface. We subsequently measured the energy required to peel a single phosphorene monolayer from a stack of black phosphorus and analyzed the role of "wedges" of solvent molecules intercalating between phosphorene sheets in initiating exfoliation. The exfoliation efficacy of a solvent is enhanced when either molecular planarity "sharpens" this molecular wedge or strong phosphorene—solvent adhesion stabilizes the newly exposed phosphorene surfaces. Finally, we examined the colloidal stability of exfoliated flakes by simulating their aggregation and showed that dispersion is favored when the cohesive energy between the molecules in the solvent monolayer confined between the phosphorene sheets is high (as with DMSO) and is hindered when the adhesion between these molecules and phosphorene is strong; the molecular planarity in solvents like DMF enhances the cohesive energy. Our results are consistent with, and provide a molecular context for, experimental exfoliation studies of phosphorene and other layered solids, and our molecular insights into the significant role of solvent molecular geometry and ordering should complement prevalent solubility-parameter-based approaches in establishing design rules for effective nanomaterial exfoliation media.

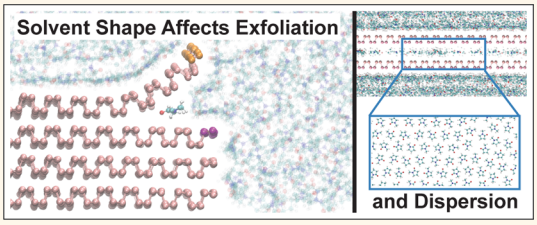

KEYWORDS: phosphorene · 2D materials · liquid-phase exfoliation · solvents · molecular dynamics · simulations

Phosphorene is a recently discovered monolayer material obtained from black phosphorus (BP). In the past 2 years, phosphorene has rapidly become the focus of a large number of research efforts motivated by the desire to develop atomically thin, two-dimensional semiconductors.[1] Unlike graphene, even unfunctionalized phosphorene possesses an intrinsic, direct band gap in mono- and multilayered forms,[2] in addition to a very high carrier mobility.[3] The resulting optoelectronic and transport properties suggest a variety of applications, including thin-film solar cells,[4] optical polarizers,[5] tunable infrared photodetectors,[6,7] nanoelectromechanical oscillators,[8] thermal management,[9] and gas sensors.[10] However, the translation of these applications of few-layer phosphorene from bench-scale prototypes to industrial and consumer device components requires the development and optimization of highly scalable preparation routes.

Fortunately, as with other van der Waals solids, phosphorene exhibits the high intralayer strength and the significantly weaker interlayer cohesion that enables top-down synthesis by cleaving layers from bulk BP. While this anisotropy is currently exploited on a bench scale by micromechanical cleavage,[11] the technique of liquid-phase exfoliation (LPE), wherein sonication-induced cavitation and shear are used to separate layers from a solvated bulk material, provides a facile and scalable method of manufacture.[12] LPE has been used to produce graphene,[13] hexagonal boron nitride (h-BN),[14] transition metal dichalcogenides,[15] and layered metal oxides,[16] and recently, several groups have employed this method to

* Address correspondence to agilio.padua@univ-bpclermont.fr, dblank@mit.edu.

Received for review May 4, 2015 and accepted July 20, 2015.

Published online July 20, 2015
10.1021/acsnano.5b02683

synthesize concentrated suspensions of electronics-grade phosphorene.[17−20]

In spite of the plethora of exfoliation media employed by various groups to date, there is still a considerable lack of knowledge on how to design the best solvent environments for exfoliation and stabilization. Thus far, LPE of nanomaterials has been studied in pure[21] and mixed[22] organic solvents, ionic liquids,[23] polymer solutions,[24] and even pure water.[25] In aqueous media, dispersants such as surfactants,[26] organic amphiphiles,[27] or other nanoparticles[28] have been tried with varying degrees of success. It is clear that the ideal exfoliation or stabilization environment depends strongly on the nature of the nanomaterial itself: cyclohexylpyrrolidinone (CHP) is excellent for exfoliating h-BN[15] but ineffective for phosphorene;[18] isopropyl alcohol (IPA) is poor at dispersing MoS_2 monolayers[29] and yet is selected to disperse phosphorene.[18] There is, therefore, a undeniable need for molecular design guidelines to enable nanotechnologists to screen through the large number of potentially useful liquid-phase environments and select the optimal solvent systems for the production and stabilization of layered nanomaterials like phosphorene.

Coleman and co-workers have suggested that the ability of a solvent to both efficiently exfoliate and disperse a given nanomaterial is linked to a close match between the cohesive energies of the nanomaterial and the solvent.[30] These cohesive energies can be quantified *via* the Hildebrand solubility parameter, a measure of a solvent's total cohesive energy per unit volume, and *via* the Hansen solubility parameters, which measure the dispersive, polar, and hydrogen-bonding components of the solvent's cohesive energy per unit volume.[31,32] According to Coleman and co-workers, the best solvents for a given nanomaterial have Hansen solubility parameters similar to those of the nanomaterial; in essence, this "like dissolves like" hypothesis attempts to correlate both exfoliation efficiency and dispersion stability with the extent to which a solvent can "dissolve" a given nanomaterial. Yet, there is evidence that both the exfoliation and the colloidal aggregation of nanomaterial flakes are linked to multiple energetic and structural details resulting from interactions between closely separated flakes and with intercalating, confined solvent molecules. Recent attempts to exfoliate graphene in organic solvents with naphthalene[33] and organic amphiphiles[27] suggest that certain moieties can act as "molecular wedges" prying open interlayer gaps during exfoliation. Additionally, efforts to stabilize nanomaterial dispersions using simple alkanes[34] and organic dyes,[35] as well as studies on solvents confined between monolayers,[36] suggest that solvent restructuring at nanomaterial surfaces and in interlayer gaps modifies, and is modified by, nanomaterial−solvent interactions.

It is not evident how to link energetic, ordering, and dynamic effects in these particular situations with macroscopic solution thermodynamics. As a result, progress in the design of solvent systems for LPE requires investigations at the microscopic scale. The search for optimal exfoliation media must be driven by an understanding of which are the key molecular descriptors—including molecular shape, bulkiness, the presence of certain chemical functional groups, or hydrogen-bonding—relevant for exfoliation and stabilization. The search for exfoliating media should be constrained to avoid toxic, impractical solvents—a real concern with graphene,[34] and the likelihood of finding a more environmentally friendly solvent system is enhanced by the consideration of a wider set of descriptors than just solubility parameters.

Molecular dynamics (MD) simulations are the best tool presently available to model the weak dispersive, polar, and hydrogen-bonding interactions that dominate solvent−nanomaterial interfaces at length and time scales relevant to LPE, with a combination of accuracy and speed unmatched by electronic structure calculations or continuum methods. Quantum density functional theory (DFT) methods do not represent electron correlation sufficiently well to represent the weak van der Waals forces accurately to the level of a few kJ/mol. Dispersion corrections can be included (DFT+D) to improve this deficiency,[37,38] but then the level of empiricism associated with the van der Waals forces becomes comparable to that of classical force fields. Besides, with DFT, the size and time scales that can be represented are still too small for the present problem. Shih *et al.* employed MD simulations in conjunction with a theory of colloidal aggregation to deduce the effects of molecular structure on the colloidal stability of graphene.[39] Kamath and Baker applied a different type of *in silico* experiment to examine the efficacies of ionic liquids for the LPE of graphene and h-BN,[40,41] and more recently, their simulation methodology has been extended to study the sliding of Bi_2Te_3 layers against each other during LPE in ionic liquids.[42] These studies have all emphasized the effects of molecular confinement on the energetics and kinetics of exfoliation and aggregation and support the need to consider the effect of the microscopic structure of the solvent phases in addition to the energetics of solubility.

RESULTS AND DISCUSSION

Here, we employ *ab initio* calculations and lattice dynamics to derive an atomistic force field capable of reproducing the interactions between widely used solvent molecules and phosphorene. We use this force field in a novel *in silico* experiment to reproduce the peeling apart of phosphorene layers during the LPE of BP in dimethyl sulfoxide (DMSO), dimethylformamide (DMF), IPA, and *N*-methyl-2-pyrrolidone (NMP). All of

these solvents have been used for LPE of several 2D nanomaterials.[15] NMP and CHP were chosen for their amide moiety and to test the effect of a bulky nonpolar substituent (cyclohexyl). IPA was chosen to test the effect of hydrogen bonding, and DMSO and DMF were chosen because they are polar aprotic solvents with high cohesive density. We subsequently study the colloidal stability of phosphorene monolayers in these solvents and describe the role of enhanced intermolecular interactions arising from the solvent molecules confined between adjacent layers in preventing aggregation.

Force Field Development. Black phosphorus has a base-centered orthorhombic structure (space group *Cmca*)[43] with a unit cell of dimensions $(a, b, c) = (3.3164, 10.484, 4.3793)$ Å. Each unit cell contains two covalently bonded layers perpendicular to the *b* lattice vector and oriented in mutually opposite directions. In this article, we will denote this direction as the *y* coordinate, so that the phosphorene layers will be aligned with the *xz* plane.

Ballone and Jones constructed an atomistic force field to reproduce the equation of state of amorphous phosphorus at high pressure and temperature.[44] Unfortunately, their use of coordination-number-dependent terms and the inability to reproduce the interatomic angles (96.4 and 102.1°) found in BP[43] indicates that this force field is not specifically tuned to represent phosphorene. Nevertheless, this force field does describe the van der Waals interactions in amorphous phases of phosphorus using Lennard-Jones potentials, and these potentials should be transferable to the interactions of phosphorene with other materials or solvents.

The intralayer potential terms in black phosphorus and phosphorene can be derived from mechanical properties. A Stillinger-Weber potential for single-layer black phosphorus has been recently parametrized based on the phonon dispersion curves obtained by quantum mechanical DFT.[45] However, this Stillinger-Weber model lacks the interlayer potentials necessary to simulate multilayer/bulk black phosphorus or the interactions with other materials or fluids.

We chose a functional form compatible with atomistic force fields of molecular solvents,[46] built on intralayer terms for covalent bonds and valence angles and van der Waals interactions between nonbonded atoms. Since the focus of this work is not on mechanical properties but rather on intermolecular forces, we opted for a simple form of the bonded potential, which consists of harmonic bonds (between pairs of covalently bonded atoms) and harmonic valence angles (involving three atoms, two of which are bonded to a central one):[47]

$$V_B = \sum_{ij}^{\text{bonds}} \frac{k_{r,ij}}{2}(r_{ij} - r_{0,ij})^2 + \sum_{ijk}^{\text{angles}} \frac{k_{\theta,ijk}}{2}(\theta_{ijk} - \theta_{0,ijk})^2 \quad (1)$$

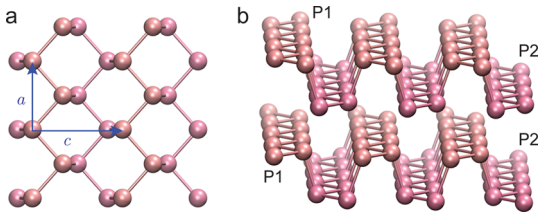

Figure 1. Crystal structure of phosphorene. (a) Lattice constants in the *xz* plane are $a = 3.3165$ Å and $c = 4.3793$ Å. (b) Phosphorus atoms in the upper (lighter colored) and lower (darker colored) planes in each phosphorene layer are labeled P1 and P2, respectively. Intraplane bonds (2.225 Å) and angles (96.4°) are smaller than their interplane counterparts (2.245 Å and 102.1°).

The nonbonded terms are represented by Lennard-Jones potentials:

$$V_{NB} = \sum_{ij}^{\text{nonbond}} 4\epsilon_{ij}\left[\left(\frac{\sigma_{ij}}{r_{ij}}\right)^{12} - \left(\frac{\sigma_{ij}}{r_{ij}}\right)^{6}\right] \quad (2)$$

where the list of nonbonded atoms includes all atoms of different layers plus atoms of the same layer separated by three or more bonds. For the particular case of atoms of the same layer separated by exactly three bonds (referred to as 1−4 interactions), the nonbonded interactions are reduced by a factor of 1/2. Due to the many possible bond paths in an extended covalent material giving rise to many values of dihedral angles, we decided not to include torsional terms in our model. Although the flexibililty of our model of phosphorene is a result of bond-stretching, angle-bending, and nonbonded potentials only, as illustrated below, our model has been parametrized to accurately reproduce the flexibility of BP reported in the literature.

In the present force field, two atom types are defined in each layer, for example, P1 in one of the planes of the puckered structure and P2 in the other, as shown in Figure 1. According to the experimental crystal structure,[43] bonds P1−P1 and P2−P2 form zigzag patterns with bond lengths of 2.225 Å and P1−P1−P1 and P2−P2−P2 angles of 96.4°. Atoms of the two planes are joined by slightly longer P1−P2 bonds of 2.245 Å, and the angles involving atoms of the two planes of the puckered structure (P1−P1−P2 and P1−P2−P2) have equilibrium values at 102.1°. The equilibrium bond lengths and angles in our model were taken from the crystal structure of BP. To reduce the computational expense of simulating phosphorene, a simpler model can be built by considering only one atom type, P, with one unique P−P bond length of 2.24 Å and one single equilibrium angle of 99.8°, sacrificing some accuracy in reproducing the experimental crystal structure.

Given its simplicity and the fact that only two force constants were fitted, the present model agrees very closely with the experimental lattice dimensions (Table 1) and agrees well with the experimental elastic constants (Table 2).[54]

TABLE 1. Force Field Parameters for Phosphorene (Å and kJ mol^{-1})[a]

parameter	atom types	value
σ	P—P	3.33
ϵ	P—P	2.0920
	P (BJ)	1.6736
r_0	P1—P1, P2—P2	2.225
	P1—P2	2.245
k_r	P—P	1720.0
θ_0	P1—P1—P1, P2—P2—P2	96.4
	P1—P1—P2, P1—P2—P2	102.1
k_θ	P—P—P	470.8

[a] P is either P1 or P2 atom types. BJ indicates the original ϵ value of the Ballone-Jones model.

TABLE 2. Comparison of Unit Cell Dimensions and Elastic Constants for BP between Calculations Using the Present Force Field and Experimental Values

Å	exptl	FF	GPa	exptl	FF
a	3.3164	3.309	C_{11}	178.6	173.1
b	10.484	10.212	C_{22}	53.6	65.9
c	4.3793	4.409	C_{33}	55.1	67.5
			C_{44}	5.5	10.9
			C_{55}	14.5	48.9
			C_{66}	21.3	16.2

The distinction between bonded and nonbonded potentials deserves some comments because it may be simplistic to consider the interlayer terms in BP to be of purely van der Waals nature. Successive layers in BP are arranged in opposite directions, which may indicate a degree of directionality in the interactions between P atoms from adjacent layers. Examining the crystal structure of BP, it is found that the shortest interatomic interlayer distances are 3.60 Å long, significantly longer than the intralayer bond distances but likely not enough to exclude some degree of orbital overlap, which can contribute to the cohesive energy of the lattice.

To clarify the nature of the interactions between layers, we performed electronic structure calculations on a periodic bilayer of BP at a series of separations. The interlayer energies obtained by (DFT+D) as well as using the atomistic force field are plotted as a function of separation in Figure 2a.

It is apparent that the Ballone-Jones model matches the dispersion term in the Grimme contribution to the DFT energies, suggesting that the Ballone-Jones force field represents the van der Waals interactions well. However, the full (DFT+D) energy is 25% higher than the dispersion term, resulting in additional cohesive energy due to the presence of significant electron density between two phosphorene layers, as can be seen in Figure 2b,c.

Therefore, the interlayer forces in BP can be more faithfully represented by a Lennard-Jones potential with an attractive well depth augmented by 25% with

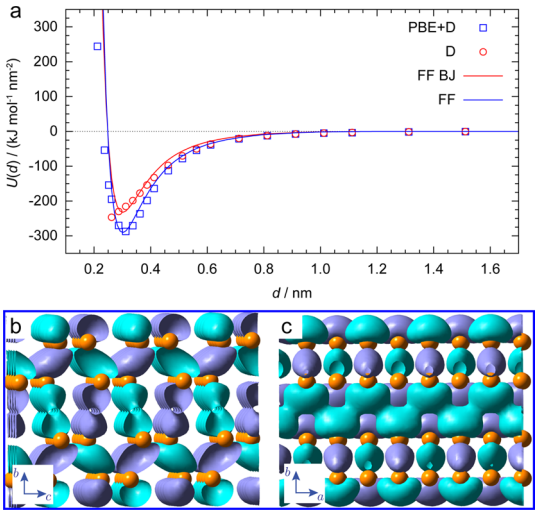

Figure 2. Interaction energy between phosphorene layers. (a) Potential energy per unit area $U(d)$ as a function of the separation distance d between two parallel phosphorene layers. The dispersive component (D) of interlayer interactions obtained from (PBE+D) DFT calculations closely matches the interlayer interaction energies predicted by the van der Waals component of the Ballone-Jones force field (FF BJ). The force field proposed in this work (FF) has been parametrized to match the full (PBE+D) energies. (b) *yz* and (c) *xy* sectional views of the interplanar orbital overlap that contributes to the interlayer interaction energy over and above dispersion. Purple and cyan represent regions where the wave function is positive and negative, respectively, with an isovalue of 0.01.

respect to the Ballone-Jones model. We adopted this augmented version in our force field for nonbonded P—P interactions in crystalline forms of BP, where stronger directional interactions are present, but retained the Ballone-Jones parameters for interactions between P materials and liquid solvents, where the interactions will be essentially of the van der Waals type. The values of the Lennard-Jones parameters are listed in Table 1.

Solvent Ordering at Phosphorene Interfaces. We studied the interactions between phosphorene and the solvents IPA, NMP, and CHP by simulating a 7 nm × 7 nm monolayer of phosphorene in simulation boxes containing each of these solvents in a *NpT* ensemble. The arrangement of solvent molecules near the interface is determined by the geometrical confinement and by the interactions between the solvents and the material: the Lennard-Jones ϵ of P atoms[48] implies that the interaction between phosphorene and carbon atoms is ≈2.5 times stronger than that between carbon atoms on neighboring solvent molecules. The ordering induced by the phosphorene surface on the solvent is illustrated by the normalized number density profiles of solvent atoms as a function of the distance normal to the monolayer (Figure 3a). In Figure 3a, the height of a curve at a given position *y* represents the ratio of the number density of solvent atoms at that position to their density in the unperturbed bulk solvent. The curves in Figure 3a are characteristic indicators of

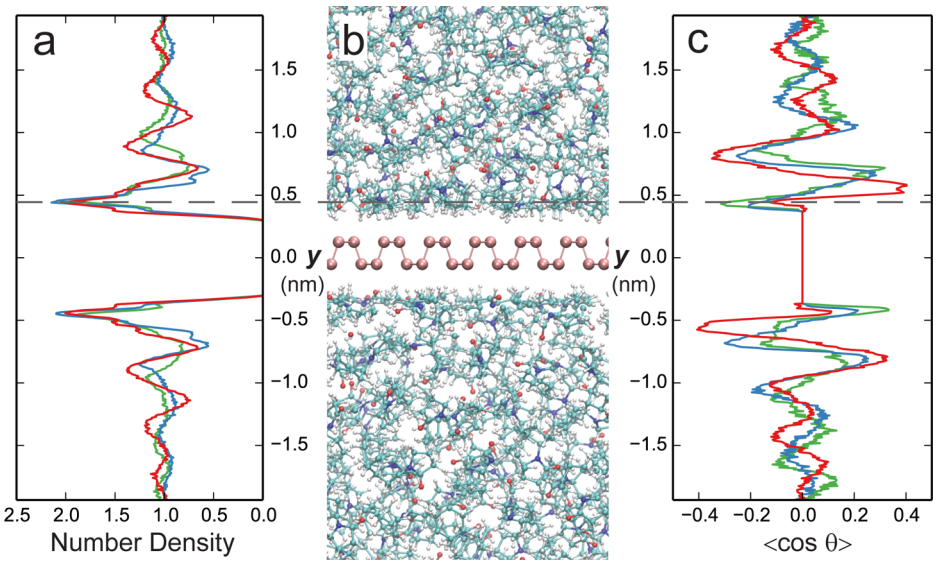

Figure 3. Solvent structure near a phosphorene monolayer. (a) Normalized number density of solvent atoms as a function of position *y* above the center of the monolayer. (b) Snapshot of a simulation box containing the phosphorene monolayer immersed in NMP. Carbon atoms are shown in cyan, nitrogen in blue, oxygen in red, and hydrogen in white. (c) Average over the *xz* plane of the cosine of the angle θ between C−O bonds and the *y* axis as a function of position *y* above the center of the monolayer. For positive *y*, a negative value of $\langle\cos\theta\rangle$ implies that the C−O bond points toward the monolayer while a positive value implies that the C−O bonds point away from the monolayer. Curves for IPA are in red, NMP in blue, and CHP in green. The dashed gray line indicates the first interfacial layer above the monolayer. The bulk densities of IPA, NMP, and CHP, as calculated from our simulations, are 0.807, 1.020, and 1.004 g/cm^3, respectively.

ordered interfacial layers (that can be observed immediately above and below the sheet in Figure 3b), with the first peaks on either side of the monolayer for all three solvents located at 0.38 nm and subsequent shells located at varying distances for each solvent until the bulk density is reached 2.0 nm away from the surface. The amplitude of the density oscillations corresponding to the subsequent solvation layers represents the degree of perturbation induced by the phosphorene surface, while their width is determined by a combination of the increased rotational freedom of solvent molecules far from the monolayer as well as by the molecular volume of the solvent. IPA appears as a more ordered liquid due to the hydrogen bonds between solvent molecules, and this results in amplitude oscillations that are more pronounced and sustained than those observed for NMP or CHP. The larger size of the CHP molecule results in oscillations with a longer wavelength, corresponding to wider solvation layers. The first peak is narrower for NMP than for CHP or IPA, indicating that the solvent atoms in the first two solvents occupy a smaller range of *y* values. This first peak is higher for NMP, implying that NMP atoms are more tightly packed into this first interfacial layer. Together, these observations suggest that the γ-lactam ring in NMP prefers to stack parallel to the phosphorene surface. The presence of two sets of rings, both of which cannot easily be coplanar alongside the phosphorene monolayer without significant torsional stress, explains the lower, wider peak in CHP. This suggests that, in the absence of conformational stress or electrostatic repulsions, ringed moieties prefer to maximize contact with the phosphorene monolayer. The presence of rings in the molecular structure can be a relevant descriptor to characterize exfoliation media.

The orientation of the solvent molecules can be ascertained by examining the angle θ between the C−O bonds in each of the three solvents and the *y* axis. The cosine of this angle averaged over the *xz* plane, $\langle\cos\theta\rangle$, as a function of the height *y* above the monolayer is shown in Figure 3c. The magnitude of the first peak is a measure of orientational ordering. In the first interfacial layer, the C−O bonds are, in general, oriented with the oxygen atoms toward the phosphorene surface, resulting in a negative peak in $\langle\cos\theta\rangle$ above the monolayer and a positive peak below the monolayer. Our results indicate that IPA molecules in the first monolayer have only slightly anisotropic orientations. IPA molecules are small and do not experience electrostatic forces from the nonpolar phosphorene monolayer. The van der Waals interaction between the hydroxyl group and phosphorene is not significantly stronger than the interactions between two methyl groups and the material. NMP molecules, on the other hand, can stack parallel to the phosphorene monolayer with the carboxy bond at orientations almost parallel to the surface, resulting in the peak observed in Figure 3c. The bulky cyclohexyl group of CHP prevents such stacking and allows the carboxyl bond more freedom to orient toward the phosphorene monolayer; this gives CHP molecules the largest $\langle\cos\theta\rangle$.

Strong secondary oscillations, with a wavelength smaller than that corresponding to the layering density,

are observed for IPA in Figure 3c—a result of alternating orientations being induced by hydrogen bonding. Similar results have been observed in simulations of the layering of water near graphite[49] and silica[50] surfaces. The corresponding oscillations for NMP and CHP have longer wavelengths, more consistent with the interfacial layering, and suggest the presence of orientational correlations that arise from longer-range dipole–dipole forces. In NMP, some authors have suggested that such forces could be supported by weak van der Waals networks.[51]

The differences observed in the orientational ordering of the solvent molecules near the phosphorene monolayer have a significant effect on the relative abilities of these solvents to exfoliate BP into phosphorene. As with other intercalation methods, LPE is initiated by the penetration of solvent molecules into the lattice structure of the bulk solid,[12] and the orientations of solvent molecules play a key role in determining the ease with which this intercalation can be achieved. Gentle exfoliation conditions are optimal in terms of both overall process energy costs and the production of larger, higher-quality monolayers.[21] Reducing the free-energy costs associated with initiating intercalation should enhance the rate of overall exfoliation. Moreover, a highly ordered interfacial layer can lead to higher barriers to aggregation, thereby promoting enhanced stability of the resulting suspensions.

Intercalation of Solvent Molecules during Liquid-Phase Exfoliation. We simulated the exfoliation of black phosphorus in the solvents DMF, DMSO, IPA, and NMP with a simulation box containing four 4 nm × 5 nm AB-stacked phosphorene monolayers immersed in solvent molecules, as shown in Figure 4a. The puckered anisotropic structure of BP affects the direction along which the peeling takes place: the stiffness of the material is anisotropic, and bending is easier along the direction of the puckers. Additionally, peeling along the *c* direction of the BP lattice exposes a gap with rectilinear upper and lower edges to solvent molecules, whereas peeling along the *a* direction exposes a gap with uneven, undulating edges that appears harder to infiltrate. Consequently, in our simulations, we peeled BP in the *bc* plane (as illustrated in Figure 4a). During these simulations, a biasing force was applied at a series of separations *d* between the edges of the uppermost phosphorene monolayer and of the monolayer immediately below it, leading to the potential of mean force (PMF). This PMF (shown in Figure 4b) represents the cumulative reversible work (the Gibbs free energy) required to peel a phosphorene monolayer from a stack of BP by pulling vertically at the leading edge.

The PMF for exfoliation in vacuum (referred to hereafter as the "vacuum PMF curve") is a smooth, monotonically increasing function of *d*, almost reaching a linear dependence with separation (indicative of steady state). If we continued the peeling trajectory up to very large separations, this PMF would approach a value of twice the surface energy of the stack of BP.

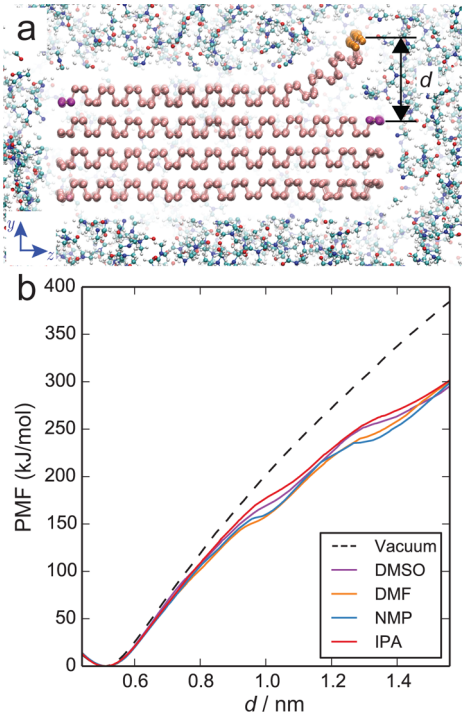

Figure 4. MD simulations of phosphorene monolayers peeled apart in vacuum, DMSO, DMF, NMP, and IPA. (a) Snapshot of the simulation box when phosphorene is exfoliated while immersed in NMP. The rows of atoms indicated in purple are restrained to their initial positions using a harmonic potential, while another harmonic is used to pull the rows of atoms indidcated in yellow in the +*y* direction. The distance between the rows indicated in yellow and the plane of the phosphorene layer immediately below them defines the reaction coordinate *d* for the peeling process. The infiltration of NMP molecules into the interlayer gap is immediately discernible. (b) PMF exerted on the phosphorene monolayer being peeled away from bulk BP as a function of *d* for the different exfoliation environments considered. These PMF curves represent the energy needed to peel the upper phosphorene layer away to a given distance *d*.

The curves that correspond to carrying out this process while immersed in solvents (referred to hereafter as the "solvent PMF curves") initially coincide with the vacuum PMF curve but quickly drop significantly lower than the vacuum PMF curve, indicating a decrease in the Gibbs free energy associated with pulling apart the edges of the layers to any given separation in a solvent relative to doing that in vacuum. The solvents considered here have a stabilizing effect on the process of creating new phosphorene surfaces; at the newly exposed surfaces, phosphorene–phosphorene interactions are replaced with new, albeit weaker, attractive phosphorene–solvent interactions. A notable property of the solvent PMF curves in Figure 4b is the series of inflection points first occurring at $d \approx 0.8$ nm and, then, more discernibly, at $d \approx 1.0$ nm and $d \approx 1.2$ nm. These modulations are characterized by

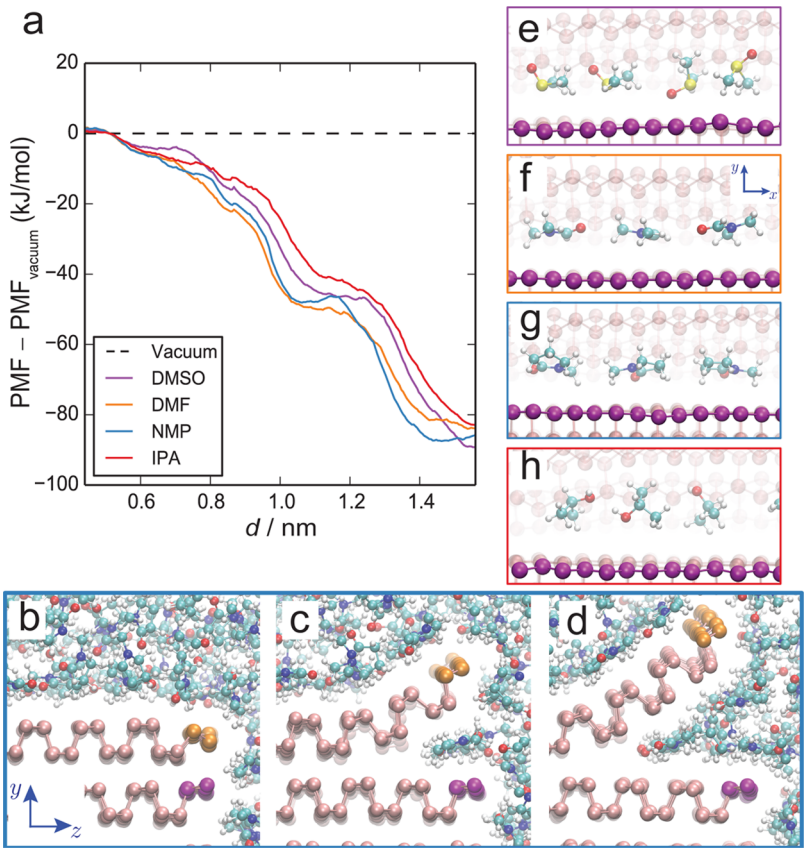

Figure 5. Intercalation of solvent molecules into the gap between phosphorene monolayers. (a) Advantage gained, in terms of the decrease in Gibbs free energy needed (kJ/mol), by peeling apart phosphorene monolayers in the different solvents we considered, as a function of the reaction coordinate *d*. (b−d) Snapshots of the infiltration of NMP molecules into the interlayer gap during the peeling apart of phosphorene as seen for *d* = 0.36, 0.95, and 1.26 nm, respectively. (e−h) Snapshots of the *xy* plane, indicating the orientation of representative solvent molecules at the leading edge of the wedge of solvent molecules occupying the gap between the phosphorene layers during exfoliation in DMSO, DMF, NMP, and IPA, respectively.

abrupt decreases in the amount of force necessary to hold the peeled monolayer in place, away from the BP stack, suggesting commensurate, sudden increases in the degree of stabilization provided by the solvent to the phosphorene layers. The inflections are related to the intrusion of solvent molecules when the successive puckers are detached.

The variations in the degree of solvent stabilization with *d* can be scrutinized by examining the difference between the solvent PMF curves and the vacuum PMF curve (Figure 5a). The corresponding evolution in the interlayer gap available for solvent intercalation and the infiltration of NMP molecules into this gap are illustrated in Figure 5b−d. Here, the inflection points seen in Figure 4b are magnified into a series of steps; the first more gradual step occurs at $d \approx 0.8$ nm, and the second and third more prominent steps occur at $d \approx 1.0$ nm and $d \approx 1.2$ nm, respectively. Each of these steps corresponds to successive steps in the process of solvent infiltration into the gap between the phosphorene layers.

For small values of *d* (*i.e.*, for $d < 0.8$ nm), the interlayer gap is not sufficiently large to allow the penetration of solvent molecules, and the difference in the solvent PMF curves remains small. For $d \approx 0.8$ nm, this interlayer gap becomes sufficiently large to enable the infiltration of the first few solvent molecules; this results in the first of the inflection points observed in the solvent PMF curves. As the interlayer gap increases from $d \approx 0.8$ nm to $d \approx 1.0$ nm, this incipient solvent infiltration results in significant decreases (to different extents) in the exfoliation PMF in the different solvents: in terms of exfoliation ease: DMF > NMP > DMSO > IPA—the intercalation of DMF molecules and IPA molecules results in the largest and smallest stabilizations with respect to the vacuum PMF, respectively. As *d* exceeds 1.0 nm, we observe the complete penetration of one layer of molecules into the interlayer gap (as seen in Figure 5c), causing the stabilizing effect to level off. Then, once again, as *d* increases to 1.2 nm (Figure 5d), the interlayer gap becomes sufficiently wide to enable the penetration of additional solvent molecules resulting in the second steep decrease in each of the solvent PMF curves. Therefore, each of these steps in the solvent PMF curve corresponds to the infiltration of successive solvation layers of molecules, providing increasing extents of van der Waals based stabilization to the newly exposed

phosphorene surfaces. This, in turn, suggests that the structural features observed in the solvation layers around an isolated phosphorene layer (Figure 3) should play a role in solvent intercalation, as well.

Representative orientations of the first group of molecules to infiltrate the interlayer gap (at 0.8 nm < d < 1.2 nm) in the case of DMSO, DMF, NMP, and IPA are illustrated in Figure 5e−h, respectively. These molecules constitute the leading edge of the wedge of solvent molecules, keeping the peeled phosphorene monolayer away from the BP stack. The atoms of representative molecules of DMF (Figure 5f) and NMP (Figure 5g) are observed to be essentially coplanar to the BP stack, with only a few hydrogen−heavy atom bonds oriented perpendicular to the layers. These orientations are consistent with the planarity of NMP molecules observed in the solvation layers around phosphorene. On the other hand, representative molecules of DMSO (Figure 5e) and IPA (Figure 5h) exhibit no such planarity—again, consistent with observations of the orientations of IPA molecules in the vicinity of a phosphorene monolayer. The planarity of molecules on the leading edge of the solvent wedge increases the sharpness of the wedge, allowing for enhanced penetration of solvent molecules into the interlayer gaps in BP and increasing the stabilization of freshly exposed phosphorene surfaces. This is, in fact, why the drop in the solvent PMF curve with respect to the vacuum PMF curve occurs always first for DMF and NMP and only at wider interlayer distances for DMSO and IPA. This increased intercalation reduces the Gibbs free energy required to initiate the exfoliation of BP and should, consequently, enhance the overall rate of exfoliation.

The trend in relative exfoliation efficacy observed in our simulations is highly consistent with experiments on the LPE of phosphorene. Yasaei *et al.* studied the performance of several solvents, including DMF, DMSO, and IPA, and concluded that DMF and DMSO were superior to IPA.[18] More recent work by Kang *et al.* confirmed prior work by Brent *et al.* that NMP was a suitable solvent for exfoliation and suggested that, prior to centrifugation (*i.e.*, in the absence of vigorous agitation), the concentration of phosphorene monolayers was higher in DMF than in NMP.[17,20]

Colloidal Stability of the Dispersed Phosphorene Sheets. Finally, the energetics and the kinetics of the aggregation of solvated phosphorene flakes are also influenced by the organization of solvent molecules in the interfacial layers, particularly of those solvent molecules confined between the aggregating flakes. The energy barriers to the solvation process are characterized by the quantity of energy needed to remove successive solvation shells from between the flakes, and these energy barriers, in turn, control the rate of the reaggregation of dispersed flakes and determine the lifetime of these colloidal suspensions.[39] To study the stability of colloidal suspensions of phosphorene, we performed MD simulations of the aggregation of two rigid 7 nm × 7 nm phosphorene monolayers oriented along the *xz* plane in the solvents DMF, DMSO, IPA, NMP, and CHP. Simulation snapshots and histograms of the solvent density as a function of the *y* coordinate for different interlayer spacings clearly illustrate the sequential removal of successive solvation shells between the monolayers (Figure 6). At separations greater than 1.3 nm, two layers of NMP molecules are found intercalated between the flakes. However, as the separation is reduced, these two layers are forced together, forming one highly confined layer of NMP molecules, with excess solvent molecules ejected from between the flakes. As the separation between the flakes becomes smaller still, solvent molecules experience large repulsive forces until, at $d \approx 0.6$ nm, no solvent molecules remain.

The van der Waals forces exerted by the phosphorene monolayers at sub-nanometer separations induce phase changes in the solvent molecules confined between them. Cross-sectional views (*xz* plane) of the confined molecules reveal an almost lattice-like structure comprising molecules that, barring in-place vibrations, show no lateral movement during the entire duration of the simulation (Figure 7a−e). Recently, observations made by Algara-Siller *et al.* suggest that water molecules confined between graphene monolayers also induce the formation of anomalous "ice-like" phases.[36] The density profile of the confined molecules perpendicular to the *y* axis indicates that the degree of planarity varies significantly across solvents (Figure 7); the density histograms for DMF and NMP are unimodal and much narrower than the corresponding histograms for IPA, DMSO, or CHP, indicating that the molecules of these two solvents adopt a much more planar configuration consistent with the planar nature of their molecular geometry. The importance of these confined, almost "frozen", solvent molecules to the energetics of the aggregation process is highlighted by the ratio of the interaction energy between these confined molecules and a phosphorene monolayer, to the interaction energy between an isolated phosphorene monolayer and all the solvent molecules around it (the configuration depicted in Figure 3b). This ratio, illustrated in Figure 7g, is quite substantial, indicating that the first solvation shell plays a vital role in determining the amount of work required to induce the reaggregation of two phosphorene flakes. The energies in Figure 7g are negative, indicating that the presence of this single confined layer is quasi-stable, with the molecules resisting displacement until the phosphorene monolayers get sufficiently close that excluded-volume interactions dominate. Furthermore, the strength of the interactions between the confined molecules and the phosphorene monolayers varies as DMF > NMP > DMSO > IPA, fully consistent with the stabilization imparted by

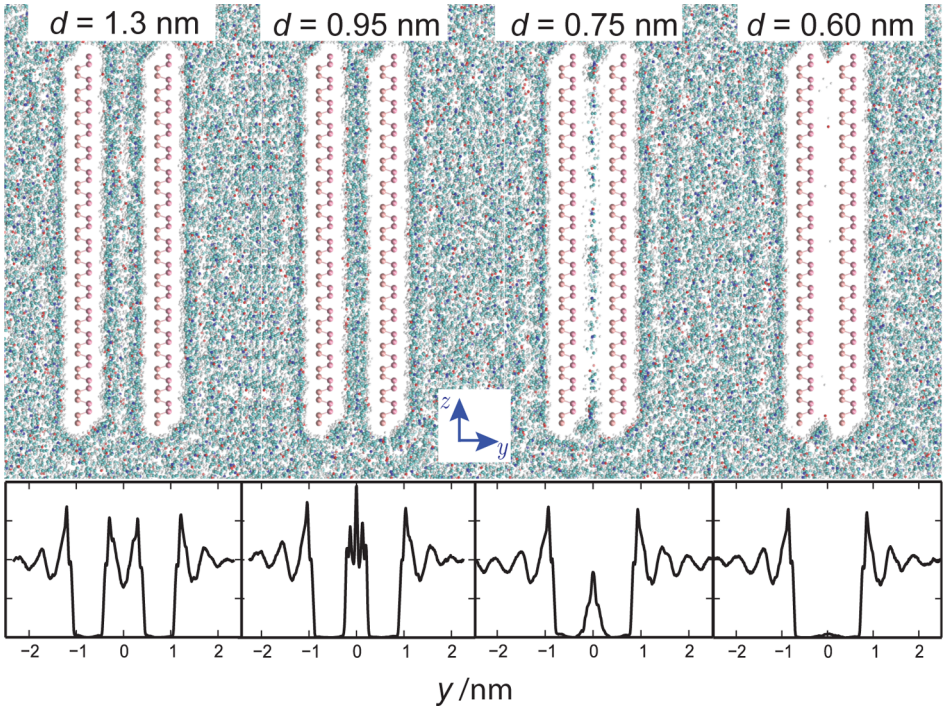

Figure 6. Cross-sectional views (*yz* plane) of NMP molecules between aggregating phosphorene monolayers for different interlayer spacings. The density of NMP molecules as a function of the *y* coordinate for different interlayer spacings indicates the removal of successive solvation shells as the phosphorene layers aggregate.

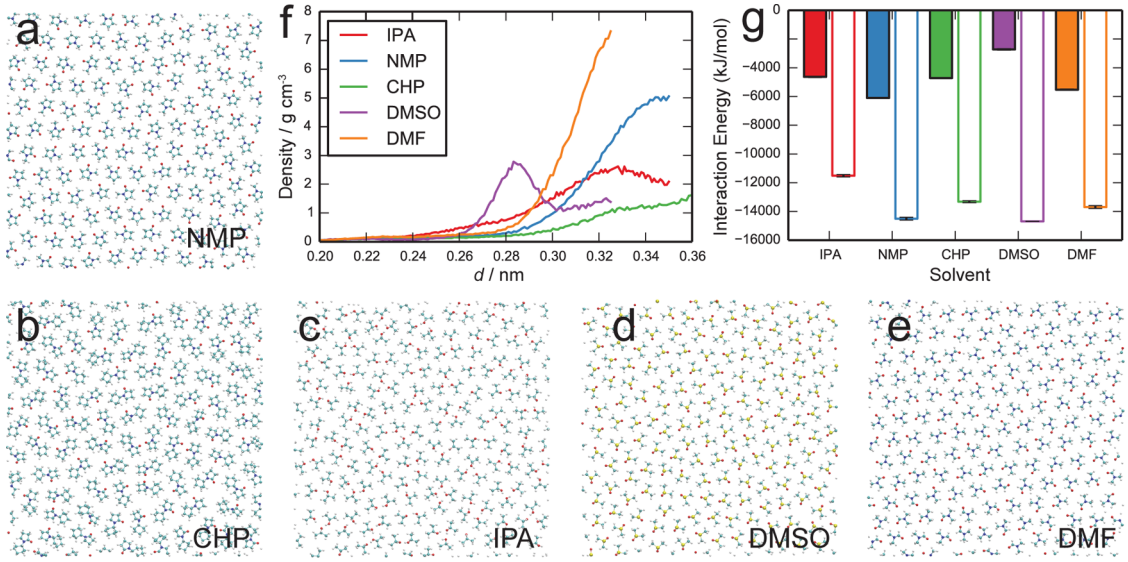

Figure 7. Organization of the solvent molecules in the final confined solvation shell between two aggregating phosphorene monolayers. The molecules in the cross-sectional (*xz* plane) views of the confined molecules of (a) NMP, (b) CHP, (c) IPA, (d) DMSO, and (e) DMF are forced to create a two-dimensional liquid crystal. (f) Density profiles of the confined molecules along the *y* axis as a function of the distance *d* from the nearest phosphorene monolayer indicates that DMF and NMP are much more planar than IPA, DMSO, or CHP. (g) Lennard-Jones interaction energy between one phosphorene monolayer and the confined molecules (colored bars) is a significant fraction of the Lennard-Jones interaction energy between one phosphorene monolayer and an unconfined slab of solvent molecules adjoining it (uncolored bars).

these solvents after the penetration of the first wedge of solvent molecules during our exfoliation simulations (Figure 5b).

We can express the amount of work required to induce two monolayers to aggregate in a given solvent, from infinite separation to a given separation *d*, as a PMF of the interactions between the monolayers (Figure 8a); the corresponding attractive forces between the monolayers are presented in Figure 8b, and the number of solvent atoms confined between the two monolayers is depicted in at smaller separations and a gradual asymptotic approach to zero as the

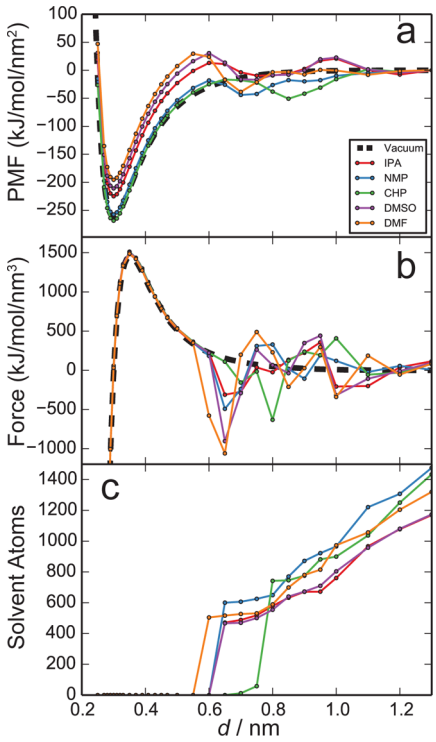

Figure 8. (a) Potential of mean force per unit area as a function of the separation *d* between two parallel phosphorene layers. (b) Force per unit area acting to pull the monolayers toward each other. (c) Numbers of solvent atoms intercalated between the phosphorene monolayers.

separation between them becomes large. Accordingly, the force driving the aggregation of these monolayers is zero at the equilibrium separation found in BP; it is negative, and large, for smaller separations, and it is positive for larger separations until it too asymptotically approaches zero as the separation becomes large.

In the presence of a solvent, the PMF curves take on additional energy minima and maxima that can be best explained by following the evolution of the numbers of atoms between the monolayers and the forces driving the aggregation as the two phosphorene monolayers approach each other. At large separations, there are multiple solvation layers characteristic of bulk solvent between the two monolayers. Consequently, the layers of solvent atoms removed at these separations, when the phosphorene monolayers begin to approach each other, are at bulk density, resulting in the linear decrease in the number of solvent atoms confined between the monolayers with decreasing separation. As the right-hand extreme of Figure 8b shows, the force required to remove these solvation layers is minimal. For separations between 1.2 and 1.0 nm, the aggregating monolayers begin to displace the final few solvation shells. The spatial discreteness of these solvation shells results in nonlinear decreases in the numbers of solvent atoms present between the phosphorene monolayers (Figure 8c). Furthermore, the creation of regions of compression and rarefaction as the solvation shells of the monolayers pass through each other induces oscillations in the force driving the aggregation (Figure 8b). These forces manifest themselves as minor oscillations in the PMF curve, with a minor maximum (*i.e.*, an energy barrier) in the curves of IPA and DMSO—solvents where comparatively stronger cohesive forces make it harder to displace the solvation shells. At separations between 1.0 and 0.8 nm, the phosphorene monolayers encounter the ultimate solvation shell in the case of the bulky CHP and the penultimate solvation shells in the case of the solvents with smaller molecules. As stressed in the context of Figure 7g, there exists a given separation at which the energy between the confined final solvation shell and the two phosphorene monolayers is negative, indicative of a quasi-stable state. The atoms of CHP confined between phosphorene monolayers at a separation of 0.85 nm represent such a state, and the energetic favorability of this state manifests itself as a significant secondary minimum in the CHP PMF curve at 0.85 nm. This last solvation shell also reveals itself in the plateau reached in the variation of atoms of CHP confined between the monolayers at d = 0.85 nm. A similar behavior is observed for the other solvents at smaller interlayer separations, as a result of the combination of their smaller molecular sizes (DMF, IPA, and DMSO) and planarity (NMP). For these solvents, the last solvation shells are at distances of ≈0.65 nm, with DMF beginning to intercalate at ≈0.6 nm. Finally, as the separations between the monolayers becomes even smaller, the final solvation shell of atoms confined between the monolayers is expelled, with the cost of expelling this shell reflected in the large negative forces shown in Figure 8b and the sizable secondary energy minimum in Figure 8a. The negative sign of the forces indicates repulsions between the phosphorene monolayers and the solvent molecules, which opposes aggregation, and the energy barrier between the secondary minimum and the deeper primary minimum represents the additional work that must be performed to force out the last solvation shell. Shih *et al.* state that the rate-determining step to the colloidal aggregation of dispersed monolayers involves overcoming this energy barrier.[39] When the last solvation shell has been expelled, the forces driving aggregation in any solvent are the same forces that drive aggregation in vacuum. Therefore, in Figure 8b, the solvent force curves coincide with the vacuum force curve at small separations.

The total work performed during the reaggregation of the phosphorene monolayers in a given solvent is the value of the corresponding PMF curve at the equilibrium separation of phosphorene layers in BP. The magnitude of this work is determined primarily by the depth of the secondary minimum and the height of the energy barrier between the secondary and the primary minima. The deeper the secondary minima, the deeper the primary minima. On the other hand, the

higher the energy barrier, the shallower the primary minima. In terms of solvent organization, the previous sentence indicates that (i) the more stable the intermediate quasi-static state, the more likely it is that phosphorene monolayers will aggregate, and (ii) the greater the force needed to disrupt this quasi-static state, the slower the aggregation. The depth of the secondary minimum is directly related to the strength of the sorptive forces between the solvent and the phosphorene monolayers. On the other hand, the height of the energy barrier is directly related to the strength of the cohesive forces operating between the solvent molecules. Consequently, the molecules of a solvent that is suitable for dispersing phosphorene should have a cohesive energy which is high enough to overcome their sorption to the phosphorene. It must be noted that the cohesive energy for a good exfoliating solvent can not be too high. Our PMF curves take as their "initial state" a system of phosphorene monolayers that have been successfully cleaved apart by the solvent. However, as shown in Figure 5a, this is only feasible if the solvent molecules overcome their mutual cohesive interactions and stabilize the newly created phosphorene surfaces.

Our simulation results indicate that NMP and CHP have deep secondary minima and low energy barriers. Indeed, the primary minimum in CHP is lower than the corresponding minimum for vacuum, suggesting that the aggregation of phosphorene monolayers in phosphorene is easier in CHP than in vacuum. This unsuitability for dispersion, combined with the lack of planarity crucial for intercalation, indicates that CHP is a poor choice for LPE. Indeed, experimental results on the LPE of phosphorene monolayers in CHP by Yasaei *et al.* are consistent with this conclusion.[18]

The PMF curves of IPA and DMSO exhibit vanishingly small secondary minima, implying weaker solvent–phosphorene interactions—an observation which is consistent with the calculated energies associated with these interactions (Figure 7g), as well as with the stabilization imparted by the wedge formed by the first solvation shell during our exfoliation simulations (Figure 5b). However, the PMF curves of these solvents exhibit larger energy barriers, indicative of the stronger intermolecular forces acting between the solvent molecules. This observation is supported by calculating the numbers of solvent *molecules* confined between the monolayers—both DMSO and IPA have more molecules in the last confined solvent shell than any of the other solvents considered. The enhanced packing of DMSO is consistent with the high cohesive energy reflected in its high boiling point, density, and viscosity. In the case of IPA, hydrogen bonding networks (seen in Figure 7c) operate between the confined molecules, contributing to its cohesive strength. Our simulation results for these two solvents are consistent with their experimental use—both solvents have been used to disperse exfoliated BP.[18]

The PMF curve of DMF exhibits not only a relatively deep secondary minimum, consistent with the large DMF–phosphorene interaction energy (see Figure 5a and Figure 7g), but also a large energy barrier between this secondary minimum and the primary minimum. This large energy barrier can be accounted for by a combination of two factors: (i) The small size and planarity of a DMF molecule enables it to remain between phosphorene monolayers even when the separation between the monolayers decreases to 0.6 nm. This resilience manifests itself as an enhanced intercalation ability (see Figure 5a). (ii) The substantial cohesive energy is also responsible for its high density, viscosity, and boiling point. The net result of these two effects is to significantly destabilize the primary energy minimum, suggesting that, of the solvents considered here, DMSO provides the optimal dispersion environment, a conclusion which is supported by several authors.[18,20]

CONCLUSIONS

In this paper, we developed and validated an interaction model for black phosphorus and phosphorene and performed three different kinds of "computer experiments" to obtain a microscopic view of phosphorene exfoliation in dimethyl sulfoxide, dimethylformamide, isopropyl alcohol, *N*-methyl-2-pyrrolidone, and *N*-cyclohexyl-2-pyrrolidone. We then studied the ordering of solvent molecules at phosphorene–solvent interfaces and calculated the free energy required to peel one phosphorene sheet from a black phosphorus stack in the presence of the solvents. Finally, we analyzed the free-energy profiles associated with the aggregation of the dispersed phosphorene flakes.

The most striking result obtained from our simulations sheds light on how the performance of a solvent depends on the shape of the molecules in the interfacial layers with phosphorene. Liquid-phase exfoliation is initiated by the penetration of a wedge of solvent molecules into the interlayer gaps, and solvents whose molecules are planar, particularly near phosphorene surfaces (such as NMP and DMSO), behave as molecular wedges that can intercalate more efficiently. Furthermore, this intercalation is successful only if the new phosphorene surfaces created by the solvent wedge are stabilized by the sorption forces between the solvent molecules and the material.

The stability of a dispersion of phosphorene sheets is favored when the cohesive energy density of solvent molecules in the last interfacial layer of solvent confined between the sheets is high and diminishes when the sorptive interactions between these confined molecules and the sheets are strong. The presence of strongly cohesive dipolar forces in solvents like DMSO

(as evidenced by its high boiling point and dipole moment[52]) and of hydrogen bonds in solvents like IPA (as evidenced by the hydrogen bonded network seen in Figure 7c) increases their suitability as stable dispersion media. Solvent planarity can further enhance dispersion stability by allowing solvent molecules to withstand a greater degree of confinement between 2D nanomaterial sheets.

Our simulations-based conclusions on the suitability of DMF, DMSO, IPA, NMP, and CHP for exfoliation and dispersion are supported by recent experimental studies.[17−20] Our conclusions are also consistent with the "like dissolves like" hypothesis proposed by Coleman *et al.*[15] Neglecting the effects of molecular planarity, our simulations show that if the adhesion between phosphorene and the solvent is stronger than the cohesion between the solvent molecules, the exfoliation of phosphorene sheets is easier but their dispersion in the solvent is more difficult. Conversely, if the cohesion between the solvent molecules is stronger than the adhesion between the solvent and phosphorene, the exfoliation of phosphorene is more difficult but the dispersion of the exfoliated sheets is easier. Therefore, if one ignores the solvent's molecular shape, the optimal liquid-phase exfoliation medium is one where the cohesion between solvent molecules is as strong as the adhesion between the solvent molecules and phosphorene.

However, our simulations also reveal the important role of planarity in explaining the superior performance of NMP and DMF, and it is hoped that these insights will contribute to a more comprehensive set of design rules, which are based not only on the energetics but also on the geometry and the ordering of solvent molecules at the interface. This more microscopic view should guide the discovery and optimization of solution environments for low agitation nanomaterial exfoliation.

METHODS

In building the force field for phosphorene, we fitted the bond-stretching and angle-bending force constants to the experimental elastic constants, using the GULP lattice dynamics code.[53] This resulted in the parameters listed in Table 1. To reduce the number of parameters that needed to be fitted, we assumed that the force constants for all bond and angle types are identical. In Table 2, we compare the unit cell dimensions and elastic constants predicted by our newly developed force field with the experimental unit cell dimensions[43] and elastic constants[54] for BP. Simulations that included torsional terms (based on dihedral angles) produced unit cell dimensions and elastic constants equivalent to those obtained using only bonds and angles. In addition, it was not feasible to resolve the contributions of angle and dihedral terms to the elastic constants. Therefore, we retained the model with the fewer fitted parameters.

Calculations of the interlayer potential energy were performed both using DFT and the classical force field. Interlayer (DFT+D) calculations were performed with the mixed Gaussian and plane-wave method[55] implemented in the CP2K code, using the PBE density functional[56] and Grimme's D3 dispersion terms.[37] The GTH pseudopotential[57] and the MOLOPT DZVP basis set[58] were used for the P atoms, arranged in a periodic supercell of $4 \times 1 \times 3$ unit cells with additional 8 Å of empty space above and below the layers (along *y*). The plane-wave grid and relative cutoffs were set at 350 Ry and 60, respectively, according to our convergence tests for an error below 5×10^{-4} kJ mol^{-1}. Calculations of the interlayer potential using the force field were performed with the LAMMPS molecular dynamics code,[59] version 10 Feb 2015, with two periodic layers of 3.97968×3.94137 nm^2 area and 4 nm of empty space above and below.

The solvents CHP, NMP, DMF, DMSO, and IPA were represented by the OPLS-AA force field.[46] The densities of these solvents, as calculated from our simulations, are 1.004, 1.020, 0.914, 1.100, and 0.807 g/cm^3, respectively, and differ from their experimentally determined counterparts by ≤4%. Parameters for the Lennard-Jones interactions between phosphorene and the solvents were obtained using geometric combining rules between the Ballone-Jones[44] parameters for P and the OPLS-AA parameters for the solvent atoms. Lennard-Jones interactions between P atoms within phosphorene had an attractive well depth ϵ scaled by 1.25 with respect to the Ballone-Jones value, according to our calculations of the binding energy between phosphorene layers, as explained in the main text.

Potential of mean force calculations with the parallel plates were carried out using GROMACS[60] version 5.0.2, with 7 nm × 7 nm phosphorene monolayers aligned in the *xy* plane in a 10 nm × 10 nm × ≈5 nm orthorhombic periodic box filled with 3301 IPA, 3170 NMP, or 1512 CHP solvent molecules, respectively. Two nanosecond long trajectories were obtained at 29 different monolayer separations using a time step of 2 fs facilitated by LINCS-constrained[61,62] hydrogen bonds. The simulations were carried out in the *NpT* ensemble, at 300 K and 1 bar, with a Nosé−Hoover thermostat with a 2.5 ps time constant and a Parinello-Rahman barostat with a 5.0 ps time constant.

Potential of mean force calculations associated with peeling one phosphorene layer from a stack were performed using LAMMPS. A stack of four phosphorene layers with dimensions of 4 nm × 5 nm aligned in the *xy* plane, in the structure of BP, was simulated in boxes filled with 2000 NMP, 2400 DMF, 2400 DMSO, or 2000 IPA molecules, respectively. Initial configurations were prepared using the FFTool[63] and Packmol[64] utilities. Molecular dynamics simulations were performed with a time step of 2 fs. Bonds terminating in H atoms were constrained using the SHAKE method.[65] A direct-space cutoff of 1.2 nm was used for both the Lennard-Jones and Coulomb potentials. Long-range electrostatic interactions were handled with the PPPM method[66] with a error below 10^{-4} in the energy. Temperature was maintained using a Nosé−Hoover thermostat[67] with time constant of 0.2 ps, and pressure was maintained by a Nosé-Hoover barostat[68,69] along *z* with a time constant of 1 ps. After equilibration, the boxes had sizes of 7 nm × 8 nm × (approximately) 6 nm along the *xyz* coordinates. This resulted in 3 nm of solvent space between periodic images of the P layers in *x* and *y* and about 4 nm of solvent along *z*. The PMF calculations proceeded by holding one edge of the top layer at a series of fixed distances from the underlying edge of the adjacent layer by a harmonic biasing force along *z*, applied to the center of mass of the edge atoms but distributed among all the edge atoms. After equilibration at each biasing point, histograms of the actual distances between the edges were accumulated during 100 ps. One histogram was obtained at every 0.05 nm at distances ranging from 0.4 to 1.6 nm between the edges (the equilibrium distance is 0.524 nm). The PMF was then calculated using the weighed histogram analysis method[70] implemented in the WHAM[71] code, converging to a tolerance of 10^{-5}. If necessary, histograms at additional points were calculated to ensure good overlap for the WHAM method to produce a very smooth PMF curve.

Conflict of Interest: The authors declare no competing financial interest.

Acknowledgment. A.P. acknowledges support from the Institut Universitaire de France and from Agence Nationale de la Recherche project CLINT (ANR-12-IS10-003). D.B. and V.S. acknowledge financial support from the National Science Foundation (CBET-1133813).

REFERENCES AND NOTES

1. Service, R. F. Beyond Graphene. *Science* **2015**, *348*, 490–492.
2. Li, L.; Yu, Y.; Ye, G. J.; Ge, Q.; Ou, X.; Wu, H.; Feng, D.; Chen, X. H.; Zhang, Y. Black Phosphorus Field-Effect Transistors. *Nat. Nanotechnol.* **2014**, *9*, 372–377.
3. Xia, F.; Wang, H.; Jia, Y. Rediscovering Black Phosphorus as an Anisotropic Layered Material for Optoelectronics and Electronics. *Nat. Commun.* **2014**, *5*, 4458.
4. Dai, J.; Zeng, X. C. Bilayer Phosphorene: Effect of Stacking Order on Bandgap and its Potential Applications in Thin-Film Solar Cells. *J. Phys. Chem. Lett.* **2014**, *5*, 1289–1293.
5. Tran, V.; Soklaski, R.; Liang, Y.; Yang, L. Layer-Controlled Band Gap and Anisotropic Excitons in Few-Layer Black Phosphorus. *Phys. Rev. B: Condens. Matter Mater. Phys.* **2014**, *89*, 235319.
6. Buscema, M.; Groenendijk, D. J.; Blanter, S. I.; Steele, G. A.; Van Der Zant, H. S. J.; Castellanos-Gomez, A. Fast and Broadband Photoresponse of Few-Layer Black Phosphorus Field-Effect Transistors. *Nano Lett.* **2014**, *14*, 3347–3352.
7. Engel, M.; Steiner, M.; Avouris, P. A Black Phosphorus Photo-Detector for Multispectral, High-Resolution Imaging. *Nano Lett.* **2014**, *14*, 6414–6417.
8. Wang, Z.; Jia, H.; Zheng, X.; Yang, R.; Wang, Z.; Ye, G. J.; Chen, X. H.; Shan, J.; Feng, P. X.-L. Black Phosphorus Nanoelectromechanical Resonators Vibrating at Very High Frequencies. *Nanoscale* **2015**, *7*, 877–884.
9. Ong, Z.-Y.; Cai, Y.; Zhang, G.; Zhang, Y.-W. Strong Thermal Transport Anisotropy and Strain Modulation in Single-Layer Phosphorene. *J. Phys. Chem. C* **2014**, *118*, 25272–25277.
10. Kou, L.; Frauenheim, T.; Chen, C. Phosphorene as a Superior Gas Sensor: Selective Adsorption and Distinct I-V Response. *J. Phys. Chem. Lett.* **2014**, *5*, 2675–2681.
11. Castellanos-Gomez, A.; Vicarelli, L.; Prada, E.; Island, J. O.; Narasimha-Acharya, K. L.; Blanter, S. I.; Groenendijk, D. J.; Buscema, M.; Steele, G. A.; Alvarez, J. V.; et al. Isolation and Characterization of Few-Layer Black Phosphorus. *2D Mater.* **2014**, *1*, 025001.
12. Nicolosi, V.; Chhowalla, M.; Kanatzidis, M. G.; Strano, M. S.; Coleman, J. N. Liquid Exfoliation of Layered Materials. *Science* **2013**, *340*, 1226419–1226419.
13. Hernandez, Y.; Nicolosi, V.; Lotya, M.; Blighe, F. M.; Sun, Z.; De, S.; McGovern, I. T.; Holland, B.; Byrne, M.; Gun'Ko, Y. K.; et al. High-Yield Production of Graphene by Liquid-Phase Exfoliation of Graphite. *Nat. Nanotechnol.* **2008**, *3*, 563–568.
14. Zhi, C.; Bando, Y.; Tang, C.; Kuwahara, H.; Golberg, D. Large-Scale Fabrication of Boron Nitride Nanosheets and their Utilization in Polymeric Composites with Improved Thermal and Mechanical Properties. *Adv. Mater.* **2009**, *21*, 2889–2893.
15. Coleman, J. N.; Lotya, M.; O'Neill, A.; Bergin, S. D.; King, P. J.; Khan, U.; Young, K.; Gaucher, A.; De, S.; Smith, R. J.; et al. Two-Dimensional Nanosheets Produced by Liquid Exfoliation of Layered Materials. *Science* **2011**, *331*, 568–571.
16. Dias, A. S.; Lima, S.; Carriazo, D.; Rives, V.; Pillinger, M.; Valente, A. A. Exfoliated Titanate, Niobate and Titanoniobate Nanosheets as Solid Acid Catalysts for the Liquid-Phase Dehydration of D-xylose into Furfural. *J. Catal.* **2006**, *244*, 230–237.
17. Brent, J. R.; Savjani, N.; Lewis, E. A.; Haigh, S. J.; Lewis, D. J.; O'Brien, P. Production of Few-Layer Phosphorene by Liquid Exfoliation of Black Phosphorus. *Chem. Commun.* **2014**, *50*, 13338–13341.
18. Yasaei, P.; Kumar, B.; Foroozan, T.; Wang, C.; Asadi, M.; Tuschel, D.; Indacochea, J. E.; Klie, R. F.; Salehi-khojin, A. High-Quality Black Phosphorus Atomic Layers by Liquid-Phase Exfoliation. *Adv. Mater.* **2015**, *27*, 1887–1892.
19. Hanlon, D.; Backes, C.; Doherty, E.; Cucinotta, C. S.; Nina, C.; Boland, C.; Lee, K.; Lynch, P.; Gholamvand, Z.; Zhang, S.; et al. Liquid Exfoliation of Solvent-Stabilised Black Phosphorus: Applications Beyond Electronics. *arXiv:1501.01881* **2015**.
20. Kang, J.; Wood, J. D.; Wells, S. A.; Lee, J.-H.; Liu, X.; Chen, K.-S.; Hersam, M. C. Solvent Exfoliation of Electronic-Grade, Two-Dimensional Black Phosphorus. *ACS Nano* **2015**, *9*, 3596–3604.
21. O'Neill, A.; Khan, U.; Nirmalraj, P. N.; Boland, J.; Coleman, J. N. Graphene Dispersion and Exfoliation in Low Boiling Point Solvents. *J. Phys. Chem. C* **2011**, *115*, 5422–5428.
22. Yi, M.; Shen, Z.; Ma, S.; Zhang, X. A Mixed-Solvent Strategy for Facile and Green Preparation of Graphene by Liquid-Phase Exfoliation of Graphite. *J. Nanopart. Res.* **2012**, *14*, 1003.
23. Liu, N.; Luo, F.; Wu, H.; Liu, Y.; Zhang, C.; Chen, J. One-Step Ionic-Liquid-Assisted Electrochemical Synthesis of Ionic-Liquid-Functionalized Graphene Sheets Directly from Graphite. *Adv. Funct. Mater.* **2008**, *18*, 1518–1525.
24. Bari, R.; Parviz, D.; Khabaz, F.; Klaassen, C. D.; Metzler, S. D.; Hansen, M. J.; Khare, R.; Green, M. J. Liquid Phase Exfoliation and Crumpling of Inorganic Nanosheets. *Phys. Chem. Chem. Phys.* **2015**, *17*, 9383–9393.
25. Li, C.; Wang, T.; Wu, Y.; Ma, F.; Zhao, G. Fabrication of Two-Dimensional Nanosheets via Water Freezing Expansion Exfoliation. *Nanotechnology* **2014**, *25*, 495302.
26. Smith, R. J.; King, P. J.; Lotya, M.; Wirtz, C.; Khan, U.; De, S.; O'Neill, A.; Duesberg, G. S.; Grunlan, J. C.; Moriarty, G.; et al. Large-Scale Exfoliation of Inorganic Layered Compounds in Aqueous Surfactant Solutions. *Adv. Mater.* **2011**, *23*, 3944–3948.
27. Park, J. S.; Yu, L.; Lee, C. S.; Shin, K.; Han, J. H. Liquid-Phase Exfoliation of Expanded Graphites into Graphene Nanoplatelets using Amphiphilic Organic Molecules. *J. Colloid Interface Sci.* **2014**, *417*, 379–384.
28. Gopalakrishnan, D.; Damien, D.; Shaijumon, M. M. MoS2 Quantum Dot-Interspersed Exfoliated MoS2 Nanosheets. *ACS Nano* **2014**, *8*, 5297–5303.
29. Cunningham, G.; Lotya, M.; Cucinotta, C. S.; Sanvito, S.; Bergin, S. D.; Menzel, R.; Shaffer, M. S. P.; Coleman, J. N. Solvent Exfoliation of Transition Metal Dichalcogenides: Dispersibility of Exfoliated Nanosheets Varies Only Weakly Between Compounds. *ACS Nano* **2012**, *6*, 3468–3480.
30. Hernandez, Y.; Lotya, M.; Rickard, D.; Bergin, S. D.; Coleman, J. N. Measurement of Multicomponent Solubility Parameters for Graphene Facilitates Solvent Discovery. *Langmuir* **2010**, *26*, 3208–3213.
31. Barton, A. F. M. *CRC Handbook of Solubility Parameters and Other Cohesion Parameters*; CRC Press: Boca Raton, FL, 1991.
32. Hansen, C. M. *Hansen Solubility Parameters: A User's Handbook*; CRC Press: Boca Raton, FL, 2007.
33. Xu, J.; Dang, D. K.; Tran, V. T.; Liu, X.; Chung, J. S.; Hur, S. H.; Choi, W. M.; Kim, E. J.; Kohl, P. A. Liquid-Phase Exfoliation of Graphene in Organic Solvents with Addition of Naphthalene. *J. Colloid Interface Sci.* **2014**, *418*, 37–42.
34. Ciesielski, A.; Haar, S.; El Gemayel, M.; Yang, H.; Clough, J.; Melinte, G.; Gobbi, M.; Orgiu, E.; Nardi, M. V.; Ligorio, G.; et al. Harnessing the Liquid-Phase Exfoliation of Graphene using Aliphatic Compounds: A Supramolecular Approach. *Angew. Chem.* **2014**, *126*, 10523–10529.
35. Schlierf, A.; Yang, H.; Gebremedhn, E.; Treossi, E.; Ortolani, L.; Chen, L.; Minoia, A.; Morandi, V.; Samorì, P.; Casiraghi, C.; et al. Nanoscale Insight into the Exfoliation Mechanism of Graphene with Organic Dyes: Effect of Charge, Dipole and Molecular Structure. *Nanoscale* **2013**, *5*, 4205–4216.
36. Algara-Siller, G.; Lehtinen, O.; Wang, F. C.; Nair, R. R.; Kaiser, U.; Wu, H. A.; Geim, A. K.; Grigorieva, I. V. Square Ice in Graphene Nanocapillaries. *Nature* **2015**, *519*, 443–445.
37. Grimme, S.; Antony, J.; Ehrlich, S.; Krieg, H. A Consistent and Accurate *ab initio* Parametrization of Density Functional Dispersion Correction (DFT-D) for the 94 Elements H-Pu. *J. Chem. Phys.* **2010**, *132*, 154104.

38. Marom, N.; Tkatchenko, A.; Rossi, M.; Gobre, V. V.; Hod, O.; Scheffler, M.; Kronik, L. Dispersion Interactions with Density-Functional Theory: Benchmarking Semiempirical and Interatomic Pairwise Corrected Density Functionals. *J. Chem. Theory Comput.* **2011**, *7*, 3944–3951.
39. Shih, C.-J.; Lin, S.; Strano, M. S.; Blankschtein, D. Understanding the Stabilization of Liquid-Phase-Exfoliated Graphene in Polar Solvents: Molecular Dynamics Simulations and Kinetic Theory of Colloid Aggregation. *J. Am. Chem. Soc.* **2010**, *132*, 14638–14648.
40. Kamath, G.; Baker, G. A. Are Ionic Liquids Suitable Media for Boron Nitride Exfoliation and Dispersion? Insight *via* Molecular Dynamics. *RSC Adv.* **2013**, *3*, 8197–8202.
41. Kamath, G.; Baker, G. A. *In Silico* Free Energy Predictions for Ionic Liquid-Assisted Exfoliation of a Graphene Bilayer Into Individual Graphene Nanosheets. *Phys. Chem. Chem. Phys.* **2012**, *14*, 7929–7933.
42. Ludwig, T.; Guo, L.; McCrary, P.; Zhang, Z.; Gordon, H.; Quan, H.; Stanton, M.; Frazier, R. M.; Rogers, R. D.; Wang, H.-T.; et al. Mechanism of Bismuth Telluride Exfoliation in an Ionic Liquid Solvent. *Langmuir* **2015**, *31*, 3644–3652.
43. Lange, S.; Schmidt, P.; Nilges, T. Au3SnP7@Black Phosphorus: An Easy Access to Black Phosphorus. *Inorg. Chem.* **2007**, *46*, 4028–4035.
44. Ballone, P.; Jones, R. O. A Reactive Force Field Simulation of Liquid−Liquid Phase Transitions in Phosphorus. *J. Chem. Phys.* **2004**, *121*, 8147–8157.
45. Jiang, J.-W.; Rabczuk, T.; Park, H. S. A Stillinger-Weber Potential for Single-Layer Black Phosphorus, and the Importance of Cross-Pucker Interactions for Negative Poisson's Ratio and Edge Stress-Induced Bending. *Nanoscale* **2014**.*7*, 6059
46. Jorgensen, W. L.; Maxwell, D. S.; Tirado-Rives, J. Development and Testing of the OPLS All-Atom Force Field on Conformational Energetics and Properties of Organic Liquids. *J. Am. Chem. Soc.* **1996**, *118*, 11225–11236.
47. McDonald, N. A.; Jorgensen, W. L. Development of an All-Atom Force Field for Heterocycles. Properties of Liquid Pyrrole, Furan, Diazoles, and Oxazoles. *J. Phys. Chem. B* **1998**, *102*, 8049–8059.
48. Ballone, P.; Jones, R. O. A Reactive Force Field Simulation of Liquid-Liquid Phase Transitions in Phosphorus. *J. Chem. Phys.* **2004**, *121*, 8147–8157.
49. Martí, J.; Nagy, G.; Guàrdia, E.; Gordillo, M. C. Molecular Dynamics Simulation of Liquid Water Confined Inside Graphite Channels: Dielectric and Dynamical Properties. *J. Phys. Chem. B* **2006**, *110*, 23987–23994.
50. Argyris, D.; Cole, D. R.; Striolo, A. Dynamic Behavior of Interfacial Water at the Silica Surface. *J. Phys. Chem. C* **2009**, *113*, 19591–19600.
51. Gontrani, L.; Caminiti, R. The Structure of Liquid N-Methyl Pyrrolidone Probed by X-Ray Scattering and Molecular Simulations. *J. Chem. Phys.* **2012**, *136*, 074505.
52. MacGregor, W. S. The Chemical and Physical Properties of DMSO. *Ann. N. Y. Acad. Sci.* **1967**, *141*, 3–12.
53. Gale, J. D. GULP: A Computer Program for the Symmetry-Adapted Simulation of Solids. *J. Chem. Soc., Faraday Trans.* **1997**, *93*, 629–637(https://nanochemistry.curtin.edu.au/gulp/) .
54. Kōzuki, Y.; Hanayama, Y.; Kimura, M.; Nishitake, T.; Endo, S. Measurement of Ultrasound Velocity in the Single Crystal of Black Phosphorus up to 3.3 GPa Gas Pressure. *J. Phys. Soc. Jpn.* **1991**, *60*, 1612–1618.
55. VandeVondele, J.; Krack, M.; Mohamed, F.; Parrinello, M.; Chassaing, T.; Hutter, J. Quickstep: Fast and Accurate Density Functional Calculations Using a Mixed Gaussian and Plane Waves Approach. *Comput. Phys. Commun.* **2005**, *167*, 103–128(http://www.cp2k.org/) .
56. Perdew, J. P.; Burke, K.; Ernzerhof, M. Generalized Gradient Approximation Made Simple. *Phys. Rev. Lett.* **1996**, *77*, 3865–3868.
57. Goedecker, S.; Teter, M.; Hutter, J. Separable Dual-Space Gaussian Pseudopotentials. *Phys. Rev. B: Condens. Matter Mater. Phys.* **1996**, *54*, 1703–1710.
58. VandeVondele, J.; Hutter, J. Gaussian Basis Sets for Accurate Calculations on Molecular Systems in Gas and Condensed Phases. *J. Chem. Phys.* **2007**, *127*, 114105.
59. Plimpton, S. J. Fast Parallel Algorithms for Short-Range Molecular Dynamics. *J. Comput. Phys.* **1995**, *117*, 1–19-(http://lammps.sandia.gov/) .
60. Van der Spoel, D.; Lindahl, E.; Hess, B.; Groenhof, G.; Mark, A. E.; Berendsen, H. J. C. GROMACS: Fast, Flexible, and Free. *J. Comput. Chem.* **2005**, *26*, 1701–1718.
61. Hess, B.; Bekker, H.; Berendsen, H. J. C.; Fraaije, J. G. E. M. LINCS: A Linear Constraint Solver for Molecular Simulations. *J. Comput. Chem.* **1997**, *18*, 1463–1472.
62. Hess, B. P-LINCS: A Parallel Linear Constraint Solver for Molecular Simulation. *J. Chem. Theory Comput.* **2008**, *4*, 116–122.
63. Pádua, A. A. H. fftool: A Tool to Build Force Field Input Files for Molecular Dynamics. 2015; https://github.com/agiliopadua/fftool.
64. Martínez, L.; Andrade, R.; Birgin, E. G.; Martínez, J. M. PACKMOL: A Package for Building Initial Configurations for Molecular Dynamics Simulations. *J. Comput. Chem.* **2009**, *30*, 2157–2164.
65. Ryckaert, J.-P.; Ciccotti, G.; Berendsen, H. J. Numerical Integration of the Cartesian Equations of Motion of a System with Constraints: Molecular Dynamics of *n*-alkanes. *J. Comput. Phys.* **1977**, *23*, 327–341.
66. Hockney, R. W.; Eastwood, J. W. *Computer Simulation Using Particles*; CRC Press: Boca Raton, FL, 1988.
67. Hoover, W. G. Canonical Dynamics: Equilibrium Phase-Space Distributions. *Phys. Rev. A: At., Mol., Opt. Phys.* **1985**, *31*, 1695–1697.
68. Parrinello, M.; Rahman, A. Crystal Structure and Pair Potentials: A Molecular Dynamics Study. *Phys. Rev. Lett.* **1980**, *45*, 1196–1199.
69. Martyna, G. J.; Tobias, D. J.; Klein, M. L. Constant Pressure Molecular Dynamics Algorithms. *J. Chem. Phys.* **1994**, *101*, 4177–4189.
70. Kumar, S.; Bouzida, D.; Swendsen, R. H.; Kollman, P. A.; Rosenberg, J. M. The Weighted Histogram Analysis Method for Free-Energy Calculations on Biomolecules. I. The Method. *J. Comput. Chem.* **1992**, *13*, 1011–1021.
71. Grossfield, A. *WHAM: The Weighted Histogram Analysis Method*, version 2.09, 2015; http://membrane.urmc.rochester.edu/content/wham.